

# Numerical Rebuilding of Plasma Wind Tunnel Experiments for Investigation of Magnetohydrodynamic Flow Interactions within the EU Project MEESST

Alessa Sperber<sup>\*†</sup>, Christian Korn<sup>\*</sup>, Omar Nimer<sup>\*</sup>, Clemens F. Kaiser<sup>\*</sup>, Johannes W. Oswald<sup>\*</sup>, Georg Herdrich<sup>\*</sup>,  
Andrea Lani<sup>\*\*</sup>, Markus Fertig<sup>\*\*\*</sup>

<sup>\*</sup> Institute of Space Systems, University of Stuttgart, Pfaffenwaldring 29, 70569 Stuttgart, Germany

<sup>\*\*</sup> Centre for mathematical Plasma Astrophysics, KU Leuven, Celestijnenlaan 200B, 3001 Leuven, Belgium

<sup>\*\*\*</sup> German Aerospace Centre, Lilienthalplatz 7, 38108 Braunschweig, Germany

sperbera@irs.uni-stuttgart.de – herdrich@irs.uni-stuttgart.de

<sup>†</sup> Corresponding Author

## Abstract

Atmospheric re-entry is a critical mission phase for crewed spaceflight and sample return missions, which requires careful study of the plasma behavior around the vehicle. This paper describes a numerical rebuilding approach for high-enthalpy plasma flows in PWT experiments with the CFD code URANUS-2D. Therefore, test conditions with high enthalpies of 60 MJ kg<sup>-1</sup> and 80 MJ kg<sup>-1</sup> were characterized, corresponding to highly elliptical and hyperbolic entry trajectories, respectively. The following report presents the numerical simulation results and their subsequent comparison to the experimental values, illustrating high levels of agreement for the highly elliptical condition and highlighting the need for further examination for the hyperbolic re-entry condition.

## 1. Introduction

There are many challenges to be met in the future of spaceflight, one of which is atmospheric re-entry, a particularly critical mission phase. With an increasing number of crewed space and sample return missions, there is a growing interest in re-entry and its associated risks. During re-entry, a plasma layer forms behind the emerging bow shock, resulting in varying degrees of dissociation and ionization of air, depending on the re-entry conditions. Furthermore, as the strong shock does not excite all internal degrees of freedom of the gas equally and the diffusion times are short compared to the relaxation times, the post shock region is in non-equilibrium during the early phase of the re-entry [1]. The velocity of the entering spacecraft is defined by the re-entry trajectory. In this paper, re-entry conditions of elliptical and hyperbolic re-entry trajectories are investigated, providing velocities of  $v_1 < v_{\infty, \text{ell}} < v_2$  and  $v_2 < v_{\infty, \text{hyp}}$ , respectively, with the first cosmic velocity  $v_1 = 7.91 \text{ km s}^{-1}$  and the second cosmic velocity  $v_2 = 11.19 \text{ km s}^{-1}$  [2]. The mass-specific enthalpy  $h_{\infty}$  of the flow during re-entry is only a function of the spacecraft velocity  $v_{\infty}$  since the internal enthalpy of the cold ambient gas can be neglected for high velocities [3]:

$$h_{\infty} = \frac{1}{2} v_{\infty}^2 \text{ for } v_{\infty} \gg 1 \text{ km s}^{-1}. \quad (1)$$

As a result, the highly elliptical re-entry condition yields a mass-specific enthalpy of  $h_{\infty, \text{ell}} = 60 \text{ MJ kg}^{-1}$  for a velocity of  $11 \text{ km s}^{-1}$ . In contrast, the Stardust re-entry capsule performing a hyperbolic re-entry at a velocity of  $12.8 \text{ km s}^{-1}$  relates to enthalpies of approximately  $80 \text{ MJ kg}^{-1}$  [3,4]. The intense heat flux on the surface of the spacecraft, resulting from the plasma layer behind the shock, is one of the primary hazards encountered during atmospheric re-entry [5]. The EU Horizon 2020 project Magnetohydrodynamic Enhanced Entry System for Space Transportation (MEESST) is developing an active magnetic shielding system utilizing High-Temperature Superconductor (HTS) coils to investigate the manipulation of the plasma through magnetohydrodynamic (MHD) effects [6]. HTS coils are expected to provide a lightweight, compact, and effective solution for the creation of the necessary magnetic field [7,8]. The resulting MHD manipulation is expected to influence the shock structure and shock standoff distance, which has been proven numerically and experimentally in previous studies [9–14]. This paper describes the numerical rebuilding of two Plasma Wind Tunnel (PWT) experiments conducted as reference scenarios without a magnetic field. For this purpose,

the proprietary 2D Computational Fluid Dynamics (CFD) code Upwind Relaxation Algorithm for Nonequilibrium Flows of the University of Stuttgart (URANUS-2D), developed at the Institute of Space Systems (IRS), is used. The simulation results are validated by comparing the stagnation heat flux and pressure with the measurement data.

## 2. Methodology

The mass-specific enthalpies described in the previous chapter are the main characterizing parameter for the re-entry condition and the PWT experiments. The experimental setup of the PWT, as well as the URANUS-2D code are presented in the following.

### 2.1 Experimental Setup

The PWT facility PWK1 of the IRS, which is used for the experiments conducted for this work, is shown in Figure 1 a). This system consists of a vacuum tank with a length of 6 m and a diameter of 2 m. The plasma source is mounted on a tank flange. Additionally, a 4-axis positioning system is integrated for the positioning of a probe in the plasma plume [15]. PWK1 incorporates the self-field magnetoplasmadynamic plasma generator (SF-MPG) RD5, which is depicted in Figure 1 b). The nozzle exit of RD5 acts as the anode, while the cathode is mounted within the plenum chamber [16]. The heating process within the SF-MPG results in partial ionization and dissociation of the test gas, which is further accelerated by the self-induced magnetic field. [17]. Consequently, RD5 produces gas flows with high enthalpies at comparatively low-pressure conditions, required for the given re-entry conditions [18].

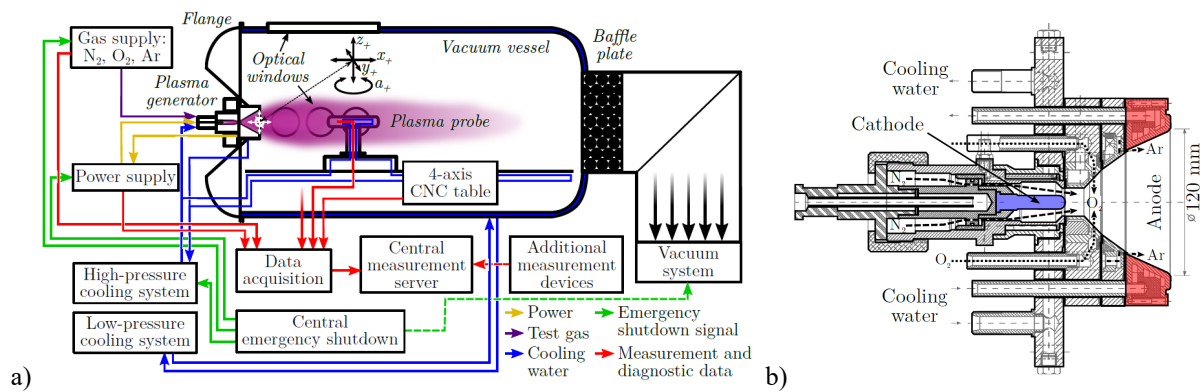


Figure 1: a) Schematic of the PWT1 test facility with the coordinate system and b) SF-MPG RD5 schematic for the experimental setup [18].

Plasma measurements during the PWT experiments are conducted using the flat-faced heat flux/pitot double probe (HF/pitot probe) with a diameter of 80 mm, depicted in Figure 2 a). The heat flux obtained from these measurements is subsequently scaled to the MHD probe geometry shown in Figure 2 b) through scaling factors based on the characteristic radii, as outlined by Oswald et al. [18].

Various PWT operating parameters are adjusted to create the necessary mass-specific enthalpies for the hyperbolic and highly elliptical re-entry conditions. These include the mass flow rates of the working gases oxygen, nitrogen and argon, the anode power, the ambient tank pressure, and the axial position of the probe in relation to the plasma generator. For the hyperbolic condition, the probe is positioned at an axial position of  $x = 300$  mm, and at  $x = 355$  mm for the highly elliptical re-entry condition. The dataset obtained through Fabry Perot interferometry from the measurements for the URANUS-2D input includes the oxygen freestream velocity and the translational temperature of atomic oxygen [18]. Additionally, the pitot pressure, the total mass-specific enthalpy, the stagnation point heat flux for the HF/Pitot probe and the ambient tank pressure are measured. The corresponding Mach numbers are derived from the pitot and tank pressure. The parameters are measured at four axial positions, precisely at  $x_1 = 200$  mm,  $x_2 = 250$  mm,  $x_3 = 300$  mm, and  $x_4 = 355$  mm. The measurements are taken at each of these positions in the radial direction, with step sizes of 10 mm between  $y = 0$  mm and  $y = 130$  mm and at  $y = 180$  mm.

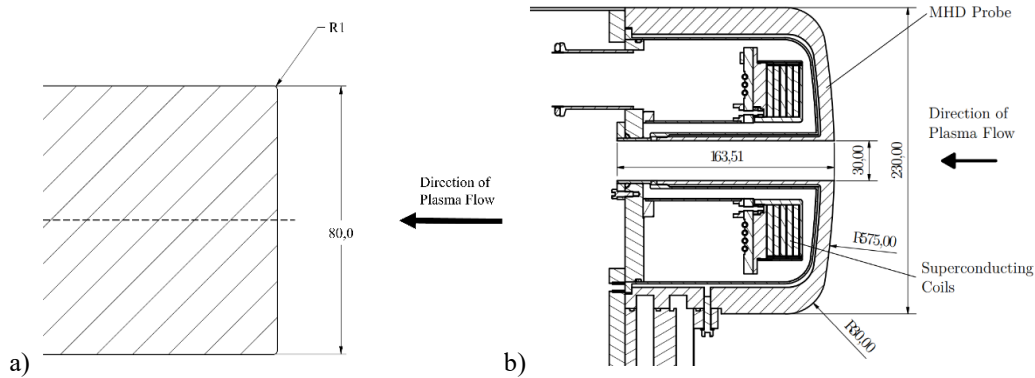


Figure 2: a) Cross section of the HF/Pitot probe (schematic representation without interior) and b) Cross section of the MHD probe (Image: J. Oswald). Lengths in [mm].

As both probe contours are numerically rebuilt with each of the defined re-entry conditions, a matrix of four test cases is defined as follows:

- Test case 1: highly elliptical condition ( $60 \text{ MJ kg}^{-1}$ ) with MHD probe,
- Test case 2: highly elliptical condition ( $60 \text{ MJ kg}^{-1}$ ) with HF/Pitot probe,
- Test case 3: hyperbolic condition ( $80 \text{ MJ kg}^{-1}$ ) with MHD probe,
- Test case 4: hyperbolic condition ( $80 \text{ MJ kg}^{-1}$ ) with HF/Pitot probe.

## 2.2 URANUS-2D Code

The axisymmetric fully coupled and fully implicit finite-volume Navier Stokes solver URANUS-2D is used for the numerical rebuilding of the defined re-entry conditions. It offers an efficient and accurate way to solve high-enthalpy flows in thermochemical non-equilibrium [19]. To account for equilibrium and non-equilibrium processes as well as relaxations, an 11 species air model ( $\text{N}_2$ ,  $\text{O}_2$ ,  $\text{NO}$ ,  $\text{N}$ ,  $\text{O}$ ,  $\text{N}_2^+$ ,  $\text{O}_2^+$ ,  $\text{NO}^+$ ,  $\text{N}^+$ ,  $\text{O}^+$  and  $e^-$ ) with 6 temperatures ( $T_{\text{tr}}$ ,  $T_{\text{vib},\text{N}_2}$ ,  $T_{\text{vib},\text{O}_2}$ ,  $T_{\text{vib},\text{NO}}$ ,  $T_{\text{rot}}$  and  $T_e$ ) is used [20]. The Navier Stokes equations (NSE) consist of 10 species continuity equations, three momentum equations, one total energy equation, three vibrational energy equations, a rotational energy equation for molecules and one equation for the energy of electrons [21]. Inviscid fluxes are discretized within the URANUS-2D solver through central differences on a structured grid and viscous fluxes through a Godunov upwind method. Second-order solutions are acquired through linear reconstruction using Total Variation Diminishing (TVD) and Weighted Essentially Non-Oscillatory (WENO) limiter extrapolation functions [22].

### Surface Modeling

For the wall boundary conditions of the NSE, two options are defined in URANUS-2D for the interaction of the flow with the surface of the probe. The first option is the no-slip condition, valid for flows with Knudsen numbers of  $\text{Kn} < 0.01$ . The second option is the slip condition with Knudsen numbers of  $0.01 < \text{Kn} < 0.1$  [23].

URANUS-2D allows for the modelling of heterogeneous catalytic recombination of atoms and ions on the surface. Therefore, fully (FC), partially (C), and non-catalytic (NC) surface models are implemented [19]. For the present investigations the global catalysis model is employed. Within this model, the recombination processes are characterized by the recombination coefficient  $0 \leq \gamma \leq 1$ , corresponding to the ratio of particles reacting on the surface to the number of particles impinging on the surface per unit of time. For fully catalytic surfaces, all atoms and ions colliding with the surface recombine ( $\gamma = 1$ ), additionally  $\text{NO}$  molecules react to  $\text{N}_2 + \text{O}_2$  [24]. In this work, a partially catalytic  $\text{CuO}$  surface is modelled with temperature and pressure dependent recombination coefficients adapted from Ballester [25]. For the measured pitot pressure of  $p_{\text{pitot}} = 480 \text{ Pa}$ , the recombination coefficients are determined to be  $\gamma_{\text{O}} = 0.2919$  and  $\gamma_{\text{N}} = 0.0824$  for the highly elliptical re-entry condition and  $\gamma_{\text{O}} = 0.33$  and  $\gamma_{\text{N}} = 0.089$  for the hyperbolic condition with  $p_{\text{pitot}} = 522.5 \text{ Pa}$ . The surface temperature of the water-cooled probe in both cases is  $T_w = 320 \pm 20 \text{ K}$ . Non-catalytic surfaces do not undergo any chemical recombination processes, and thus are modelled with  $\gamma = 0$ . Ion recombination is an important consideration for C and FC surfaces, particularly for hyperbolic re-entry conditions. However, numerical instabilities throughout the simulations prevented the modeling of ion recombination.

### 3. Numerical Rebuilding Approach

This chapter outlines the numerical rebuilding approach, including the definition of the computational area and numerical grid for the different test cases, as well as the processing of the experimental data and the resulting inflow conditions for the URANUS-2D solver. The numerical simulations are executed based on the assumptions and definitions given in this chapter.

#### 3.1 CEA Approximation

Not all inflow parameters required for the URANUS-2D simulations can be obtained from the measurements. Consequently, the Chemical Equilibrium with Applications (CEA) solver [26] was used for the calculation of the missing data. The CEA solver is a 0D thermal equilibrium solver developed by NASA to estimate the thermochemistry for high-temperature applications. It should be noted that chemical equilibrium is assumed in CEA, which may cause deviations in the simulation results from the PWT measurements. As inputs, CEA requires the molar fractions of the reacting species, in this case N<sub>2</sub> and O<sub>2</sub>, the pressure and specific molar enthalpies. The determination of the molar enthalpies in the outer radial area ( $y \geq 130$  mm) is subject to inaccuracies, since the PWT measurements are associated with high uncertainties. To address this issue, a Gauss fit was applied to the measured enthalpies prior to the calculations with CEA for the reduction of measurement noise. In addition, the enthalpies used for the CEA calculation of the thermochemical state are iteratively reduced by the kinetic portion that is not considered [27]. The molar mass fractions of the species, the mean molar mass, the density of the gas mixture and the equilibrium temperature are then calculated through CEA. Furthermore, the local sonic velocity is obtained and used for the calculation of the flow velocity with the experimental Mach numbers.

#### 3.2 Boundary Conditions

For the resolution of the computational domain, URANUS-2D requires a structured grid with four distinct boundaries. Figure 4 shows an example of the computational area with its corresponding boundaries for the MHD probe flow simulation. Symmetry conditions must be fulfilled along the x-axis. Furthermore, specifying the inflow parameters for each cell along the inflow boundary is possible. For URANUS-2D, the pressure, the partial mass densities of the species, the inflow velocity and the flow angle are required. Additionally, five of the six temperatures must be defined directly, including the three vibrational temperatures, the rotational temperature, and the electron temperature. The translational temperature is calculated internally from the provided input parameters.

These parameters are determined from experimental data in combination with the CEA calculation results. The inflow pressure is set equal to the ambient pressure of  $p = 175$  Pa and the temperature components are set equal to the determined equilibrium temperature ( $T_{\text{eq}} = T_{\text{vib.N}_2} = T_{\text{vib.O}_2} = T_{\text{vib.NO}} = T_{\text{rot}} = T_e$ ), which is shown in Figure 3 a) in radial direction up to  $y = 180$  mm. The inflow velocity for all test cases is defined through a weighted average of the CEA-calculated flow velocity and the velocity measured in the PWT experiments, as shown in Figure 3 b) in radial direction. The trust values of the weighting matrix are thereby chosen in favor of the measurement values.

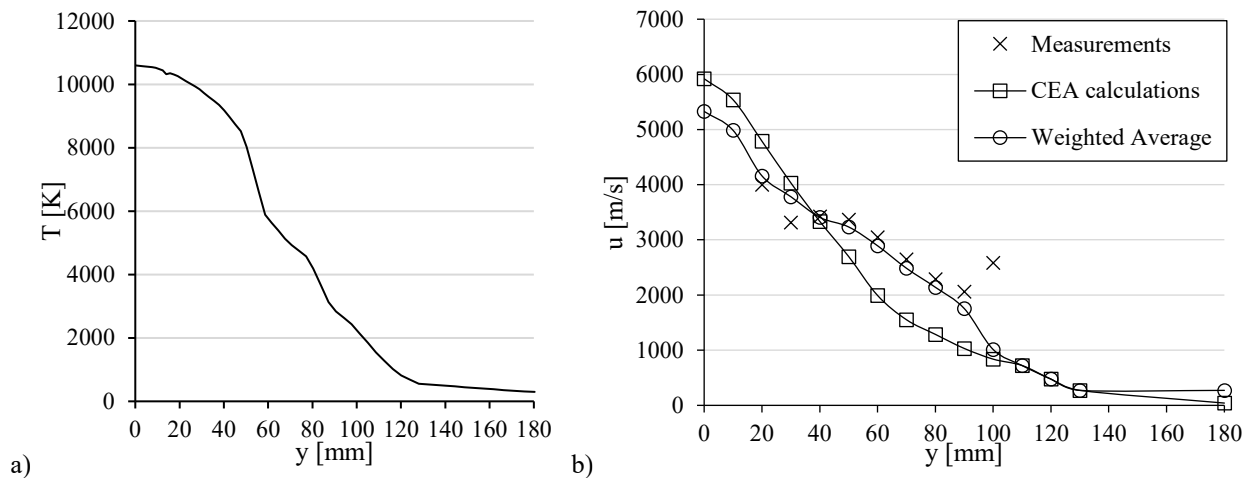


Figure 3: a) Inflow temperature distribution and b) emergence of the weighted average velocity distribution in radial direction through measurements and CEA calculations.

It should be noted that the values for the velocity remain constant throughout  $y = 130$  mm due to a truncation of the radial velocity distribution at this point. For the temperature distribution, the truncation is applied at  $y = 180$  mm, resulting in a minimum temperature of  $T_{\min} = 298.5$  K.

For the outflow boundary, the flow parameters can be extrapolated from the cells closest to the boundary. However, it is important to note that this approach is only valid in computational domains with sufficient depth to mitigate the impact of gradients or shocks on the outflow boundary [22]. For the wall boundary, the slip condition is chosen (see section 2.2) with a wall temperature of  $T_w = 320$  K unless otherwise specified.

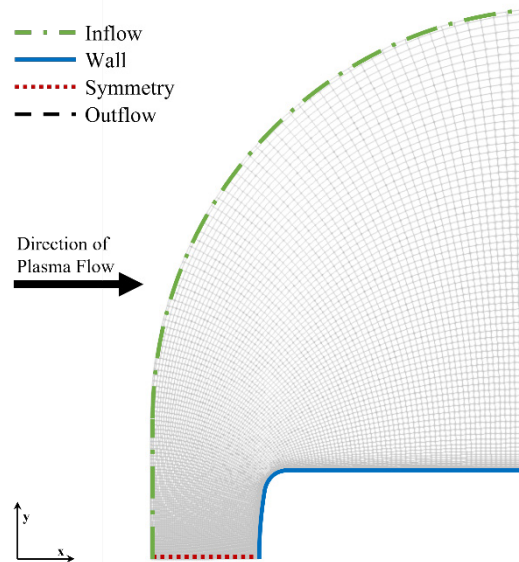


Figure 4: Computational area and boundaries defined for the MHD probe.

### 3.3 Numerical Grids

This chapter presents the numerical grids used for the different PWT conditions. Therefore, Figure 5 visually represents the grids used for both probes in the test cases 1 and 2.

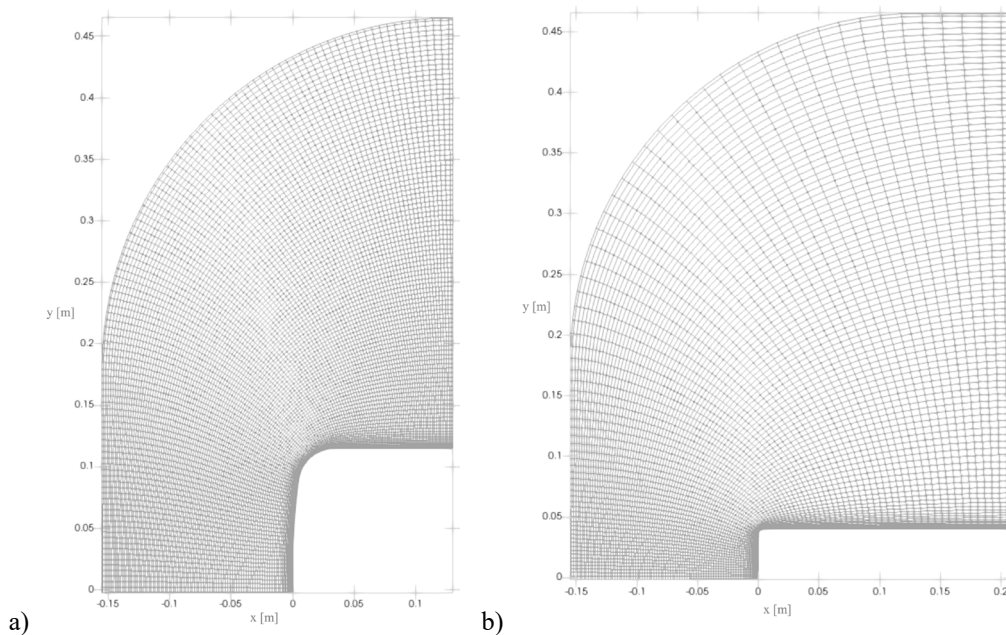


Figure 5: Numerical grids for a) test case 1 and b) test case 2.

Different grids are used for the individual test cases as the relative position of the inflow boundary to the probe surface changes. Additionally, the grid used for the MHD probe simulation stands out in terms of height, given that the hyperbolic condition for the MHD probe is expected to have larger gradients, and the flow deviations caused by the proximity of the probe to the inflow are anticipated to be more significant. Additional grid refinement is applied on the symmetry line in front of the MHD probe in the radial direction, with a surface normal resolution of 1 mm and a growth ratio of 1.02, to mitigate high gradients. Figure 6 depicts the grids for both probes in the hyperbolic test cases 3 and 4.

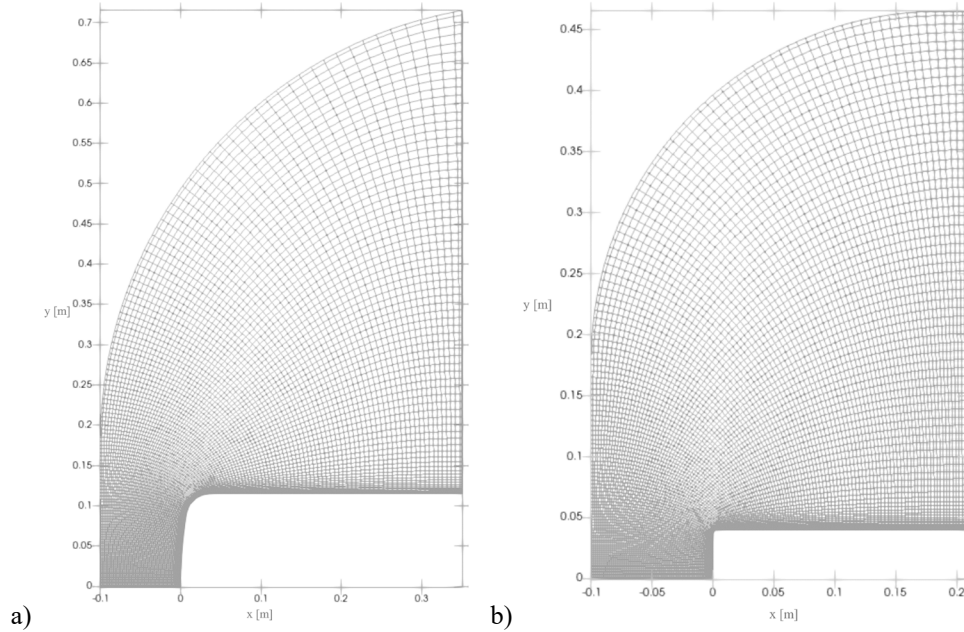


Figure 6: Numerical grids for a) test case 3 and b) test case 4.

Table 1 provides the parameters for the introduced grids, including the number of cells indicated as [“cells along the surface” x “cells perpendicular to the surface”]. It is apparent that the MHD probe requires more cells along the surface due to its larger diameter.

Table 1: Numerical grid parameters for all defined test cases.

Test case	1	2	3	4
Number of Cells	110x105 (11550 Cells)	70x101 (7070 Cells)	129x79 (10191 Cells)	93x71 (6603 Cells)
Surface Normal Resolution	0.05 mm	0.05 mm	0.1 mm	0.1 mm
Growth Ratio	1.05	1.05	1.2	1.1

#### 4. Numerical Simulations

This chapter elucidates the simulation results of the four test cases. The simulations are performed with NC, C, and FC surface conditions for the MHD and the HF/Pitot probe. The NC and FC simulations represent the polarizing cases and, therefore, the range of the minimum and maximum simulation outcomes concerning surface modeling. Further, the simulation results are validated against the experimental PWT measurements using the stagnation pressure and heat flux.

## 4.1 Results

In the following sections, the results of the highly elliptical and the hyperbolic re-entry conditions are given and described.

### 4.1.1 Highly Elliptical Re-entry Condition

For the highly elliptical re-entry condition, the pressure and Mach number distributions with a contour line at  $Ma = 1$  are presented in Figure 7. Here, the C surface condition is considered for both probe geometries. For the calculation of the Mach number in URANUS-2D, an isentropic exponent of  $\kappa = 5/3$  is obtained due to the non-equilibrium assumption for chemistry and internal degrees of freedom.

The plasma beam is clearly visible through the supersonic inflow in this area. As the MHD probe provides a much larger diameter than the plasma jet, stronger deflections of the incident flow and higher tangential velocities occur compared to the HF/pitot probe. The emerging shock is assumed to be a weak shock due to the low gradients, especially visible in the pressure distributed flow fields (see Figure 7 c) and d)). In addition, Mach numbers of  $Ma > 1$  can be observed in the flow fields throughout the pressure increase, which is indicative for a weak shock.

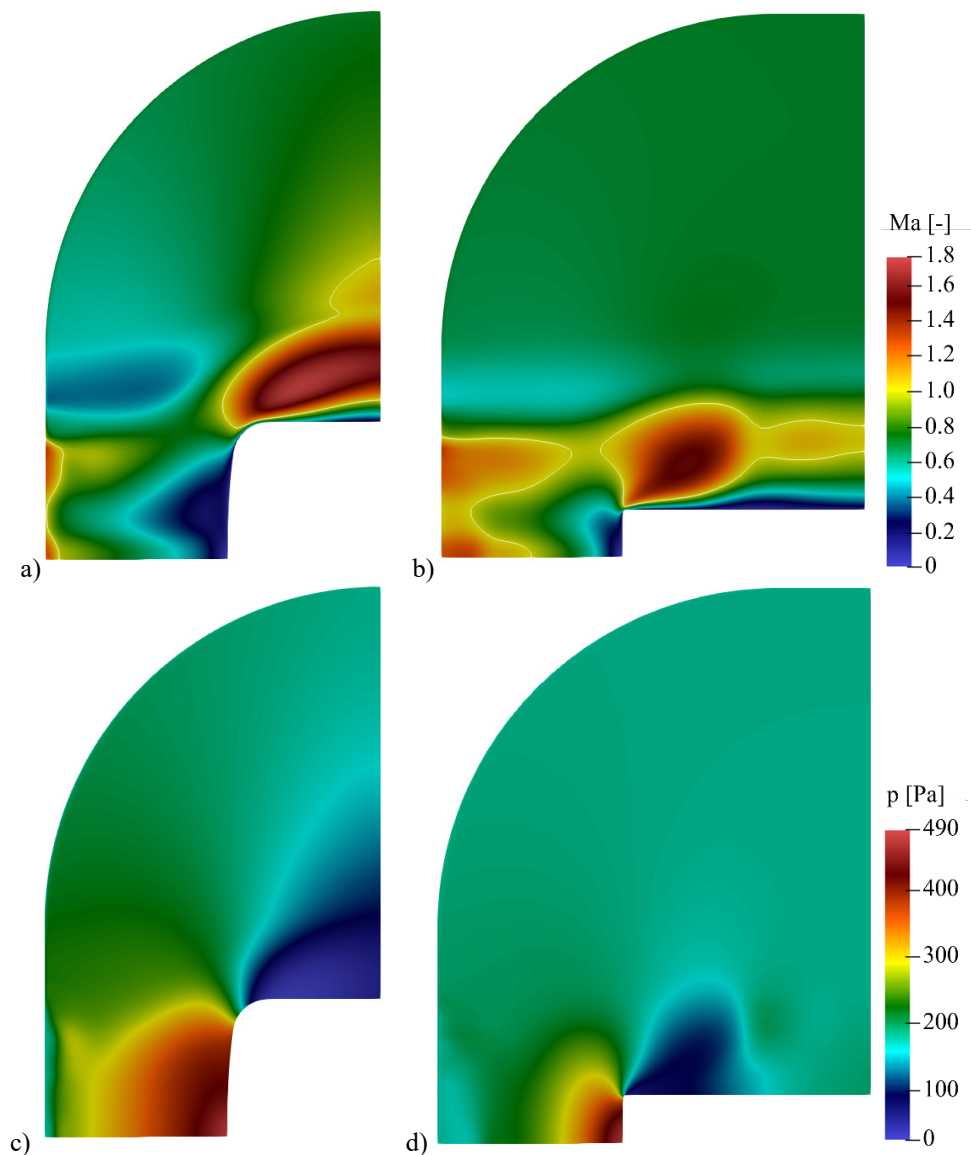


Figure 7: a), b) Visualizations of the Mach number distributions with isolines at  $Ma = 1$  for test cases 1 and 2, respectively. c), d) Pressure distribution for test cases 1 and 2, respectively.

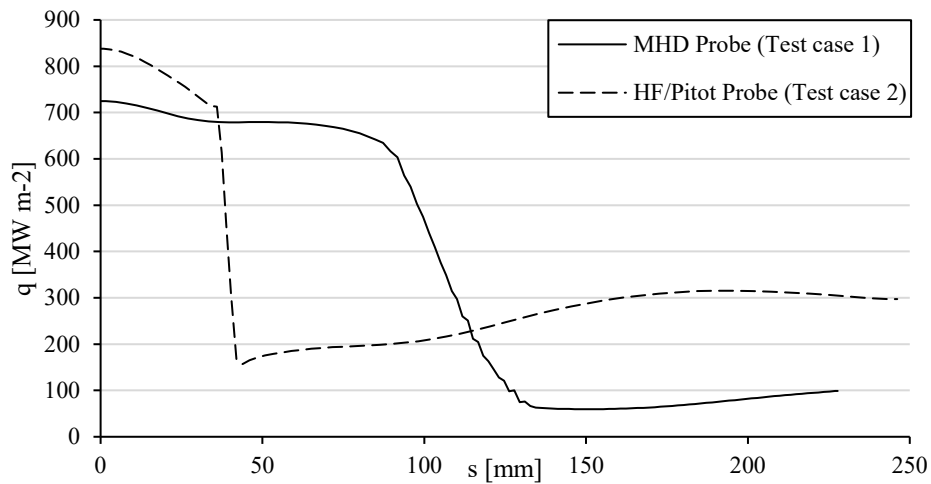


Figure 8: Heat flux over the surface coordinate  $s$  of the different probes in test cases 1 and 2.

The emerging compression area in front of the probe is influenced by the probe diameter, resulting in a greater area for the MHD probe. The position of the shock is influenced by the compression area and the transonic Mach numbers, resulting in a high standoff distance especially for the MHD probe. From the results provided by URANUS-2D, the shock distance can be determined on the symmetry line to distances at  $d_{s,1} = 143.4$  mm and  $d_{s,2} = 78.0$  mm from the surface for the test cases 1 and 2, respectively.

Figure 8 shows the heat flux of the different probe geometries for the highly elliptical condition versus the surface coordinate of the probe. For the HF/pitot probe, a sudden decrease in the heat flux is visible at the shoulder of the probe at  $s \approx 40$  mm. As the MHD provides a more rounded shoulder, the decrease in the heat flux takes place more continuously at  $s \approx 100 \dots 130$  mm. Additionally, the heat flux on the surface of the probe behind the shoulder area is significantly higher for the HF/pitot probe due to the smaller size of the probe and the resulting positioning of the horizontal surface in more intense areas of the plasma beam.

#### 4.1.2 Hyperbolic Re-entry Condition

For the hyperbolic test cases 3 and 4, the Mach number and pressure-distributed flow fields for the different probes are displayed in Figure 9, with contour lines drawn for  $Ma = 1$  for the Mach number. The shock distances for the test cases 3 and 4 are  $d_{s,3} = 98.3$  mm and  $d_{s,4} = 76.2$  mm from the surface, respectively.

Additionally, the heat fluxes over the surfaces of the different probes for the hyperbolic re-entry condition are shown in Figure 10. In contrast to the highly elliptical condition, the computed heat flux in the stagnation area for the MHD probe is higher than for the HF/pitot probe. As this behavior is not indicated by the measurements, the results of these test cases should be replicated and further investigated. The heat flux of the MHD probe also increases faster downstream the shoulder region but remains at approximately the same value for the rear part of the probe. This is also visible for the behavior of the heat flux of the HF/pitot probe.

One important difference between the highly elliptical and the hyperbolic condition is the size of the computational area between the probe and the inflow boundary. For test case 4 with the HF/pitot probe, providing only a slight increase in the shock distance compared to test case 2, this limitation is not significant. However, for the MHD probe in test case 3, this results in the positioning of the shock at a distance of 1.7 mm from the inflow boundary. Compared to the highly elliptical test case 1, with  $d_{s,1} = 143.4$  mm, the actual position of the shock may be outside the computational area for this test case, which can lead to high inaccuracies in the simulation results.

Similar distributions are observed for the NC and FC conditions, which can be found in Korn [27], Nimer et al. [28], and Sperber [29].

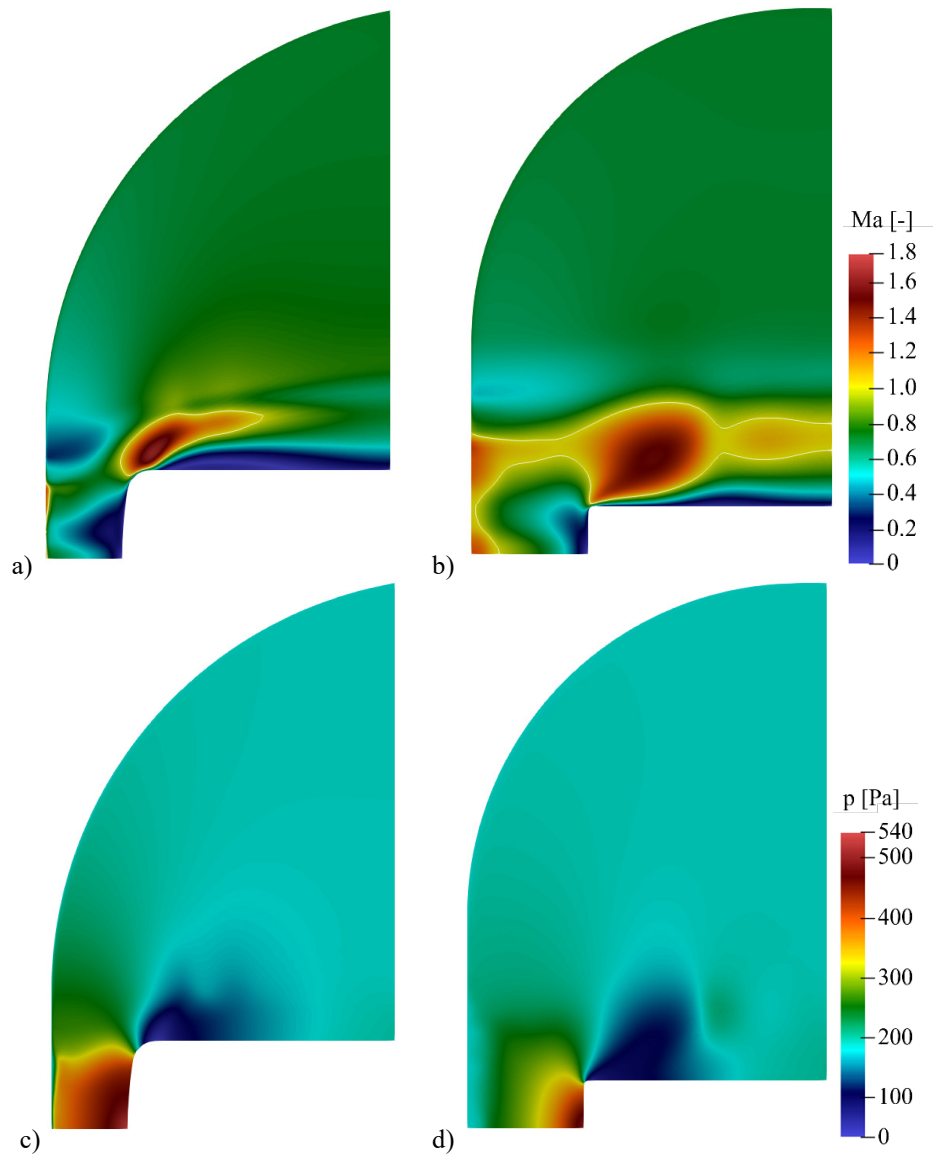


Figure 9: a), b) Visualizations of the Mach number distributions with isolines at  $Ma = 1$  for test cases 3 and 4, respectively. c), d) Pressure distribution for test cases 3 and 4, respectively.

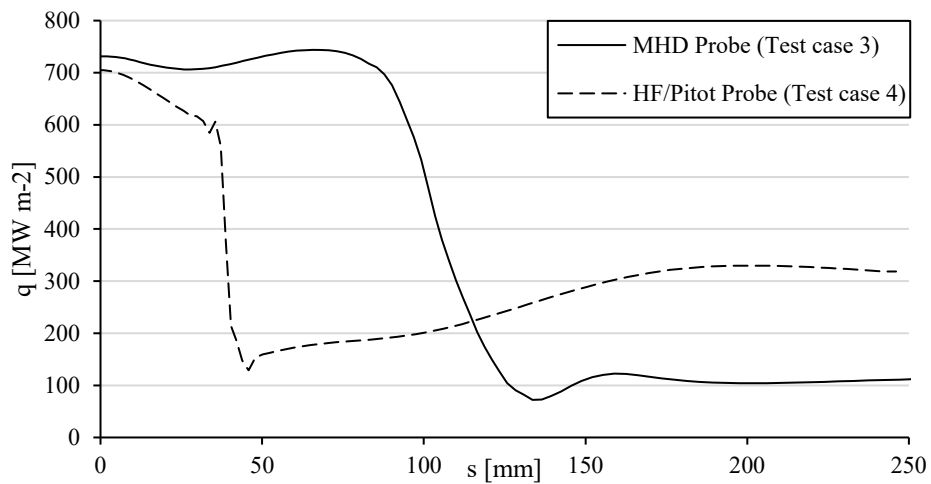


Figure 10: Heat flux over the surface coordinate  $s$  of the different probes in Test cases 3 and 4.

## 4.2 Validation against the Experimental Database

This chapter focuses on the validation of the simulation results of the four defined test cases against the experimental database using two key metrics: stagnation pressure ( $p_{\text{stag}}$ ) and heat flux ( $q_{\text{stag}}$ ). The comparison of simulation results against these metrics allows for a reliable assessment of the simulation's accuracy. The accuracy is quantified by calculating the respective absolute and relative percentual errors. The respective absolute error

$$\varepsilon_i = |i_{\text{PWT}} - i_{\text{sim}}|, \quad i \in [q_{\text{stag}}, p_{\text{stag}}] \quad (2)$$

compares the stagnation values of the PWT with the simulation results (sim) directly, while

$$\delta_i = \frac{|i_{\text{PWT}} - i_{\text{sim}}|}{i_{\text{PWT}}} * 100\%, \quad i \in [q_{\text{stag}}, p_{\text{stag}}] \quad (3)$$

represents the relative error. The NC and FC simulations are considered additionally to the C results for the validation.

### 4.2.1 Highly Elliptical Re-entry Condition

This section provides and discusses the results of the highly elliptical re-entry condition. Therefore, the highly elliptical re-entry condition is subdivided into the simulations of the MHD and the HF/Pitot probe, corresponding to test cases 1 and 2.

#### MHD Probe

Table 2 presents the simulation results of test case 1 compared to the PWT measurements scaled to the MHD probe geometry. The scaled values from the experiment in the stagnation point lie within the range of the simulation results from the NC and FC cases. The simulation under the C condition exhibits an absolute deviation of  $\varepsilon_q = 26.6 \text{ kW m}^{-2}$  and a relative deviation of  $\delta_q = 3.8\%$  from the measurements. Based on this consistency, it can be concluded that this simulation is the most accurate in terms of replicating the measurement values. The simulations conducted for the NC and C cases have shown a slight overestimation of pressure by less than 2.0%. The significant influence of the catalysis modeling on the surface heat flux can be seen from the fact that the heat flux is three times higher in the FC case compared to the NC case. In the context of the catalysis model, it is worth noting that the ion recombination, which is presently not taken into account, may influence the simulation results for the C case.

Additional inaccuracies may arise from implementing the scaling function used to determine the experimental heat flux for the MHD probe. Further deviations occur for all simulations, as the results are influenced by the CEA approximation described in the previous chapter. The numerical parameters such as the type of limiter used, and the approximate Riemann solver employed can influence the solution as well. To reduce complexity, the simulations were conducted without radiative coupling, which can cause additional deviations. However, despite these considerations, the simulation results of this test case are in good agreement with the PWT measurement data.

Table 2: Simulation results for the MHD probe at the stagnation point for the highly elliptical condition. The heat flux and pressure are compared to the PWT measurements by absolute and relative errors.

Parameter	Unit	NC Simulation $T_w = 320 \text{ K}$	C Simulation $T_w = 320 \text{ K}$	FC Simulation $T_w = 320 \text{ K}$	Scaled PWT Measurements
Heat flux $q_{\text{stag}}$	$[\text{kW m}^{-2}]$	522.6	724.7	1612.2	$698.1 \pm 59.4$
Absolute heat flux error $\varepsilon_q$	$[\text{kW m}^{-2}]$	175.5	26.6	914.1	-
Relative heat flux error $\delta_q$	$[\%]$	25.1	3.8	130.9	-
Pressure $p_{\text{stag}}$	$[\text{Pa}]$	487.7	489.5	474.9	$480.3 \pm 1.2$
Absolute pressure error $\varepsilon_p$	$[\text{Pa}]$	7.4	9.2	5.4	-
Relative pressure error $\delta_p$	$[\%]$	1.5	1.9	1.1	-

#### HF/Pitot Probe

The HF/Pitot probe simulation results are summarized and compared to the PWT measurements in Table 3. In this case, the measured values at the stagnation point fall within the range of the NC and FC cases as well. However, for the C condition, there is a notable underestimation of measured heat flux by  $\varepsilon_q = 306.1 \text{ kW m}^{-2}$ , resulting in a percentual deviation of  $\delta_q = 26.8 \%$ . It is noticeable that the deviation from the experimental values for this case is higher than that of the MHD probe. The simulation results of the HF/Pitot probe yield pressure data that is in very good agreement with the measurements. The absolute error is  $\varepsilon_p = 2.0 \text{ Pa}$ , which is equivalent to a relative error of  $\delta_p = 0.4\%$  from the pressure obtained through PWT measurements. However, it may be necessary to make some adjustments for the heat flux rebuilding to further improve the precision.

Table 3: Simulation results for the HF/Pitot probe at the stagnation point for the highly elliptical condition. The heat flux and pressure are compared to the PWT measurements by absolute and relative errors.

Parameter	Unit	NC Simulation	C Simulation	FC Simulation	PWT
		$T_w = 320 \text{ K}$	$T_w = 320 \text{ K}$	$T_w = 320 \text{ K}$	Measurements
Heat flux $q_{\text{stag}}$	$[\text{kW m}^{-2}]$	624.3	837.8	2182.8	$1143.9 \pm 25.5$
Absolute heat flux error $\varepsilon_q$	$[\text{kW m}^{-2}]$	519.6	306.1	1038.9	-
Relative heat flux error $\delta_q$	$[\%]$	46.0	26.8	90.8	-
Pressure $p_{\text{stag}}$	$[\text{Pa}]$	480.6	482.3	473.1	$480.3 \pm 1.2$
Absolute pressure error $\varepsilon_p$	$[\text{Pa}]$	0.3	2.0	7.2	-
Relative pressure error $\delta_p$	$[\%]$	0.0	0.4	1.5	-

#### 4.2.2 Hyperbolic Re-entry Condition

This section presents the findings of the hyperbolic re-entry condition, including the MHD and the HF/Pitot probe simulations.

##### MHD Probe

The stagnation point values and associated errors for the MHD probe are given in Table 4. Again, the C simulation provides the highest agreement with the PWT measurements. The absolute deviation of the heat flux observed in this case is  $\varepsilon_q = 241.5 \text{ kW m}^{-2}$ , corresponding to a relative deviation of  $\delta_q = 24.8\%$ . Upon analysis of the simulation results, a slight overestimation of the pressure by 3.8% is evident in both the NC and C cases compared to the measurement data. While this level of inaccuracy is considered acceptable, the simulation results for the heat flux exhibit a significant deviation. It is assumed that these discrepancies are mainly caused by the positioning of the shock front at the inflow boundary. In order to determine the actual position of the shock and thus obtain more reliable results, the distance between the inflow boundary and the probe geometry must be increased. Therefore, the definition of a new dataset through PWT measurements is required. However, the probe cannot be moved arbitrarily close to the plasma generator due to mechanical limits of the components and the maximum temperature of the cooling water within the probe. Because the dataset described in this work is already inaccurate due to the CEA approximation and the weighted average conducted for the inflow velocity determination, an extrapolation approach does not appear reasonable as an alternative solution. As a result, further investigation is required especially regarding the feasibility of PWT measurements with decreased distance between the MPG and the probe. The impact of ion recombination should be considered in a revised surface catalysis model as well to reduce the deviations from the measurement values. It should further be noted that the proximity of the probe and the SF-MPG during the PWT measurements may have resulted in interactions between these components, which are not rebuilt within the URANUS-2D solver.

Table 4: Simulation results for the MHD probe at the stagnation point for the hyperbolic condition. The stagnation heat flux and pressure are compared to the PWT measurements by absolute and relative errors.

Parameter	Unit	NC Simulation $T_w = 320 K$	C Simulation $T_w = 320 K$	FC Simulation $T_w = 320 K$	Scaled PWT Measurements
Heat flux $q_{\text{stag}}$	[kW m <sup>-2</sup> ]	554.7	731.7	1891.5	973.2 ± 81.8
Absolute heat flux error $\epsilon_q$	[kW m <sup>-2</sup> ]	418.5	241.5	918.3	-
Relative heat flux error $\delta_q$	[%]	43.0	24.8	94.4	-
Pressure $p_{\text{stag}}$	[Pa]	542.4	542.1	522.5	522.5 ± 1.3
Absolute pressure error $\epsilon_p$	[Pa]	19.9	19.6	0.0	-
Relative pressure error $\delta_p$	[%]	3.8	3.8	0.0	-

### HF/Pitot Probe

Table 5 provides the stagnation point values and corresponding errors for the HF/Pitot probe from test case 4. In the C case, the measured heat flux is underestimated by  $\epsilon_q = 889.9 \text{ kW m}^{-2}$  resulting in a percentual deviation of  $\delta_q = 55.8\%$ . The deviation from experimental values in this case is even more significant than for the MHD probe. Although the distance between the shock and the inflow boundary is increased for this test case, the interaction thereof can cause deviations. In addition, a comparison of NC simulations from test cases 2 and 4 indicates that test case 2 results in a higher level of heat flux at the stagnation point, contrary to the experimental measurements. Furthermore, test case 4 indicates a slightly higher heat flux (difference of  $27.5 \text{ kW m}^{-2}$ ) for the FC case with a wall temperature of  $T_w = 2000 \text{ K}$ . However, this scenario is not representative due to the anticipated decline in heat flux when the wall temperature is lowered to  $320 \text{ K}$ . Overall, these findings suggest that the highly elliptical test cases 1 and 2 are in better agreement with the PWT measurements, and more investigation is needed for the hyperbolic test cases 3 and 4.

Table 5: Simulation results for the HF/Pitot probe at the stagnation point for the hyperbolic condition. The heat flux and pressure are compared to the PWT data by absolute and relative errors.

Parameter	Unit	NC Simulation $T_w = 320 K$	C Simulation $T_w = 320 K$	FC Simulation $T_w = 2000 K$	PWT Measurements
Heat flux $q_{\text{stag}}$	[kW m <sup>-2</sup> ]	550.1	704.9	2471.1	1594.8 ± 28.1
Absolute heat flux error $\epsilon_q$	[kW m <sup>-2</sup> ]	1044.7	889.9	876.3	-
Relative heat flux error $\delta_q$	[%]	65.5	55.8	54.9	-
Pressure $p_{\text{stag}}$	[Pa]	496.8	498.1	477.4	522.5 ± 1.3
Absolute pressure error $\epsilon_p$	[Pa]	25.7	24.4	45.1	-
Relative pressure error $\delta_p$	[%]	4.9	4.7	8.6	-

## 5. Conclusion

This paper outlined a numerical rebuilding approach for the analyzation of high-enthalpy flows of PWT experiments. This study identified two distinct atmospheric re-entry conditions based on their characteristic enthalpies. An enthalpy of  $60 \text{ MJ kg}^{-1}$  characterizes the highly elliptical re-entry condition, while the hyperbolic re-entry condition corresponds to an enthalpy of  $80 \text{ MJ kg}^{-1}$ . The numerical simulations were performed using URANUS-2D, an axisymmetric, fully

implicit Navier-Stokes solver developed at IRS. Following the visual representation of simulation results with the MHD and HF/Pitot probes, the stagnation pressure and heat flux values were compared to PWT experimental measurements. Regarding the simulation of the highly elliptical conditions with the MHD and HF/Pitot probes, it was found that the former yielded a better agreement with the experimental measurements. In contrast, the latter provided less agreement, particularly with respect to the heat flux. Additionally, the resulting heat fluxes from simulations with hyperbolic simulations deviated more significantly from the PWT measurements compared to the highly elliptical condition. It was presumed that the reason of the high deviations is especially the small distance between the inflow boundary and the probe geometry for the hyperbolic re-entry condition. As a result, measurements for the determination of the inflow conditions at greater distances from the probe would allow better simulations. Additional improvements can be achieved by further adaption of the numerical grids to the flow and an increased number of cells in radial direction, as well as the consideration of ion recombination in the surface catalysis modeling.

## 6. Acknowledgements

This project has received funding from the European Union's Horizon 2020 Research and Innovation Program under grant agreement 899298. This paper only reflects the author's view, and the European Commission is not responsible for any use that may be made of the information it contains.

## References

- [1] Behte, H. A., and E. Teller. 1953. Deviations from thermal Equilibrium in Shock Waves. Technical Report. University of Michigan, Engineering Research Institute.
- [2] Messerschmid, E., and S. Fasoulas. 2017. Raumfahrtsysteme. Eine Einführung mit Übungen und Lösungen, 5<sup>th</sup> ed., Springer Vieweg.
- [3] Herdrich, G., Fertig, M., and S. Löhle. 2009. Experimental Simulation of High Enthalpy Planetary Entries. *The Open Plasma Physics Journal*. 2:150–164.
- [4] Desai, P. N., Mitcheltree, R. A., and F. M. Cheatwood. 1999. Entry Dispersion Analysis for the Stardust Comet Sample Return Capsule. *Journal of Spacecraft and Rockets*. 36:463–469. DOI: 10.2514/2.3467
- [5] Cap, F. 1994. Lehrbuch der Plasmaphysik und Magnetohydrodynamik, Springer Verlag.
- [6] "Magnetohydrodynamic Enhanced Entry System for Space Transportation," URL: <https://meesst.eu/> [retrieved 3 November 2022].
- [7] La Rosa Betancourt, M., Collier-Wright, M., Bögel, E., Lozano, J. M., Lani, A., et al. 2021. MEESST as a key building block for low-cost interplanetary missions. *Journal of the British Interplanetary Society*. 74:448–453.
- [8] Collier-Wright, M., La Rosa Betancourt, M., Herdrich, G., Bögel, E., and A. Behnke. 2022. High-temperature superconductor based power and propulsion system architectures as enablers for high power missions, *Acta Astronautica*. 201:198–208. DOI: 10.1016/j.actaastro.2022.08.035
- [9] Müller, R. A., Pagan, A. S., Upadhyay, P. P., and G. Herdrich. 2019. Numerical Assessment of Magnetohydrodynamic Heat Flux Mitigation for Pico-Sized Entry Capsule Mockup. *Journal of Thermodynamics and Heat Transfer*.
- [10] Sharma, V., Giangaspero, V. F., Donaldson, N. L., Giacomelli, J., Lani, A., et al. 2022. Numerical Modeling Verification for Re-Entry Vehicles using Enhanced MHD Simulation Tools. In: *73rd International Astronautical Congress*.
- [11] Giacomelli, J., Herdrich, G., Oswald, J. W., Pagan, A. S., Behnke, A., et al. 2021. Experimental and Numerical Studies of MHD Effects on Plasma Flows for Re-Entry Applications. In: *72nd International Astronautical Congress*.
- [12] Knapp, A. 2012. Investigation of MHD Impact on Argon Plasma Flows by Variation of Magnetic Flux Density. *The Open Plasma Physics Journal*. 5:11–22. DOI: 10.2174/1876534301205010011
- [13] Kranc, S. C. 1969. Experimental Investigation of Magnetohydrodynamic Flow around Blunt Bodies. PhD Thesis. Northwestern University.
- [14] Fujino, T. and M. Ishikawa. 2006. Numerical Simulation of control of plasma flow with magnetic field for thermal protection in Earth reentry flight. *IEEE Transactions on Plasma Science*. 34:409–420. DOI: 10.1109/tps.2006.872458
- [15] Herdrich, G., Auweter-Kurtz, M., Endlich, P., Löhle, S., Pidán, S., et al. 2004. IRS Ground-Testing Facilities: Thermal Protection System Development, Code Validation and Flight Experiment Development. In: *24th Aerodynamic Measurement Technology and Ground Testing Conference*.
- [16] Auweter-Kurtz, M., Laure, S., and W. Röck. 1994. Experimental Planet Entry Simulation within a Plasma Wind Tunnel. In: *2nd European Symposium on Aerothermodynamics for Space Vehicles*, 429–436.

- [17] Laure, S. H., Auweter-Kurtz, M., Fasoulas, S., Habiger, H. A., and W. Röck. 1992. The IRS plasma wind tunnels as a tool for the investigation of planet entry missions. In: *17th AIAA Aerospace Ground Testing*.
- [18] Oswald, J. W., Herdrich, G., Pagan, A. S., Behnke, A., and J. Giacomelli. 2022. Evaluation of high enthalpy air plasma conditions for investigation of magnetohydrodynamic flow interactions. In: *2nd International Conference on Flight Vehicles, Aerothermodynamics and Re-entry Missions & Engineering*.
- [19] Frühauf, H. H., Fertig, M., Olawsky, F., and T. Bönisch. 2000. Upwind Relaxation Algorithm for Re-entry Nonequilibrium Flows. Krause, E., and W. Jäger (eds.) *High Performance Computing in Science and Engineering '99*, Springer Verlag. 365–378.
- [20] Fertig, M. and G. Herdrich. 2009. The Advanced URANUS-2D Navier-Stokes Code for the Simulation of Nonequilibrium Re-entry Flows. *Trans. JSASS Aerospace Tech. Japan*, 7:15–24.
- [21] Ballester, B. M., Pidan, S., Herdrich, G., and M. Fertig. 2015. Recent catalysis measurements at IRS. *Advances in Space Research*. 65:742–765. DOI: 10.1016/j.asr.2015.04.028
- [22] Fertig, M. 2005. Modellierung reaktiver Prozesse auf Siliziumkarbid-Oberflächen in verdünnten Nichtgleichgewichts-Luftströmungen. PhD Thesis. University of Stuttgart, Institute of Space Systems.
- [23] Karniadakis, G., Beşkök, A., and N. Aluru. 2005. Microflows and nanoflows. Fundamentals and simulation. Springer.
- [24] Balat, M., Czerniak, M., and J. Badie. 1997. Thermal and chemical approaches for oxygen catalytic recombination evaluation on ceramic materials at high temperature. *Applied Surface Science*. 120:225–238.
- [25] Ballester, B. M. 2019. Aerothermochemistry of High-Temperature Materials for Atmospheric Entry. PhD Thesis. University of Stuttgart, Institute of Space Systems.
- [26] NASA Glenn Research Center, “Chemical Equilibrium with Applications,” URL: <https://www1.grc.nasa.gov/research-and-engineering/ceaweb/> [retrieved 30 March 2023].
- [27] Korn, C. 2023. Numerical Rebuilding of Highly Elliptical Re-entry Test Cases within the EU Project MEESST. Master Thesis. University of Stuttgart, Institute of Space Systems.
- [28] Nimer, O., Oswald, J. W., Korn, C., Herdrich, G., Sharma, V., et al. 2023 [unpublished]. Magnetohydrodynamic Enhanced Entry System for Space Transportation Deliverable D3.1: Validation results for heat flux w/o magnet. Technical Report, EU MEESST.
- [29] Sperber, A. 2023. Numerical Rebuilding of Hyperbolic Re-Entry Test Cases within the EU Project MEESST. Master Thesis. University of Stuttgart, Institute of Space Systems.